

# RELIABLE PROBABILITY FORECAST OF SOLAR FLARES: DEEP FLARE NET-RELIABLE (DeFN-R)

Naoto Nishizuka<sup>1</sup>, Yûki Kubo<sup>1</sup>, Komei Sugiura<sup>2,3</sup>, Mitsue Den<sup>1</sup> and Mamoru Ishii<sup>1</sup>

## ABSTRACT

We developed a reliable probabilistic solar flare forecasting model using a deep neural network, named Deep Flare Net-Reliable (DeFN-R). The model can predict the maximum classes of flares that occur in the following 24 h after observing images, along with the event occurrence probability. We detected active regions from  $3 \times 10^5$  solar images taken during 2010–2015 by Solar Dynamic Observatory and extracted 79 features for each region, which we annotated with flare occurrence labels of X-, M-, and C-classes. The extracted features are the same as used by Nishizuka et al. (2018); for example, line-of-sight/vector magnetograms in the photosphere, brightening in the corona, and the X-ray emissivity 1 and 2 h before an image. We adopted a chronological split of the database into two for training and testing in an operational setting: the dataset in 2010–2014 for training and the one in 2015 for testing. DeFN-R is composed of multilayer perceptrons formed by batch normalizations and skip connections. By tuning optimization methods, DeFN-R was trained to optimize the Brier skill score (BSS). As a result, we achieved  $BSS = 0.41$  for  $\geq C$ -class flare predictions and 0.30 for  $\geq M$ -class flare predictions by improving the reliability diagram while keeping the relative operating characteristic curve almost the same. Note that DeFN is optimized for deterministic prediction, which is determined with a normalized threshold of 50%. On the other hand, DeFN-R is optimized for a probability forecast based on the observation event rate, whose probability threshold can be selected according to users' purposes.

*Subject headings:* magnetic fields — methods: statistical — Sun: activity — Sun: chromosphere — Sun: flares — Sun: X-rays, gamma rays

---

<sup>1</sup>Applied Electromagnetic Research Institute, National Institute of Information and Communications Technology, 4-2-1, Nukui-Kitamachi, Koganei, Tokyo 184-8795, Japan; nishizuka.naoto@nict.go.jp

<sup>2</sup>Department of Information and Computer Science, Keio University, 3-14-1 Hiyoshi, Kohoku, Yokohama, Kanagawa 223-8522, Japan

<sup>3</sup>Advanced Speech Translation Research and Development Promotion Center, National Institute of Information and Communications Technology

## 1. Introduction

Solar flare prediction is a long-standing problem in solar physics and astrophysics. The fundamental physical process of solar flares has been unveiled by recent theoretical and observational studies, but neither a standard approach to predict flares nor understanding of the mechanism of flare occurrence has been established. There are four approaches to flare prediction: (i) empirical human forecasting, (ii) statistical method, (iii) machine learning method, and (iv) numerical simulation by solving physical equations. Each model has been developed to predict categories or occurrence probabilities of flares in the following 24 h. Since the number of large-class flares is much smaller than that of small-class flares or non-flare events, flare prediction is an imbalanced problem.

Probability forecasts are widely used in human forecasting (Crown 2012; Devos et al. 2014; Murray et al. 2017), as well as in statistical methods (Wheatland 2000; Moon et al. 2001; Gallagher et al. 2002; Wheatland 2005; Lee et al. 2012; Bloomfield et al. 2012, 2016; Lee et al. 2016; McCloskey et al. 2016, 2018; Leka et al. 2018; Lim et al. 2019a,b). It is more convenient to show the occurrence probability for each class of flares rather than the deterministic one when the observation is near the border of two categories. Ideally, the forecast probability is equal to the observation event rate. The prediction result is often evaluated by the relative (receiver) operating characteristic (ROC) curve (Swets 1973; Mason 1982; Stanski et al. 1989; Harvey et al. 1992), the reliability diagram, and the Brier skill score (BSS). BSS uses the climatological event rate as a reference forecast and is complemented by a reliability diagram that compares the forecast probabilities and the observation frequency. Barnes (2016) compared eleven probability forecasting models of solar flares and concluded that several of them lack reliability (see also Leka et al. 2019; Park et al. 2020).

On the other hand, it is currently popular to apply machine learning algorithms to predict categories of flares occurring in the following 24 h. In previous works, classical algorithms such as neural networks (Qahwaji & Colak 2007; Colak & Qahwaji 2009; Higgins et al. 2011; Ahmed et al. 2013), support vector machines (SVMs; Qahwaji & Colak 2007; Yuan et al. 2010; Al-Ghraibah et al. 2015; Bobra & Couvidat 2015; Boucheron et al. 2015; Muranushi et al. 2015; Raboonik et al. 2017; Sadykov & Kosovichev 2017; Alipour et al. 2019), the least absolute shrinkage and selection operator (LASSO; Benvenuto et al. 2018; Jonas et al. 2018), random forests (RFs; Liu et al. 2017; Florios et al. 2018; Wang et al. 2019; Campi et al. 2019), extremely randomized trees, which is an extension of the RF model with higher accuracy (ERTs; Nishizuka et al. 2017), and an unsupervised fuzzy clustering (Benvenuto et al. 2018) were applied to flare prediction. They are trained to increase a skill score, such as the true skill statistic (TSS), also known as the Peirce skill score, or the Hanssen and Kuipers discriminant (H&KSS). TSS has an advantage of not depending on the ratio of positive and neg-

ative events in the database, as well as the odds ratio skill score and the symmetric extremal dependence index. Furthermore, deep neural networks (DNNs) have also recently been applied and have succeeded in improving TSS (Huang et al. 2018; Nishizuka et al. 2018; Park et al. 2018; Liu et al. 2019; Chen et al. 2019; Zheng et al. 2019; Domijan et al. 2019; Yi et al. 2020; Li et al. 2020; Panos & Kleint 2020).

Machine-learning-based forecast algorithms including DNNs, which were trained to increase TSS, show forecast results with higher TSS values but lower BSS values and lack reliability (Barnes et al. 2016). The reliability diagrams show a systematic over-forecast for larger occurrence probability. Unreliable probabilistic forecast models are often calibrated by the terrestrial weather forecast community (e.g., Gneiting et al. 2007; Primo et al. 2009), but such calibration is not popular in the space weather forecast community. Instead, each model is requested to directly forecast solar flares reliably. However, a useful optimization method employing machine learning algorithms to realize the probability forecast of solar flares with high reliability has not yet been discussed. It has been mathematically verified that for reliable prediction models, TSS is maximized at the probability threshold of the climatological event rate, while the converse is not obvious (Kubo 2019).

In this study, we investigated optimization methods to realize reliable probabilistic forecasts by machine learning algorithms. We improved our prediction model of solar flares using DNNs, named Deep Flare Net (DeFN; Nishizuka et al. 2018) to obtain reliable probability forecasts, and we renamed it Deep Flare Net-Reliable (DeFN-R). In sections 2 and 3, we describe our model and datasets. The prediction results are explained in section 4 and summarized in section 5, with discussion of the optimization method suitable for producing reliable models.

## 2. Overview of DeFN-R

### 2.1. General Explanation of Model

We used a solar flare prediction model employing DNNs named DeFN to investigate how to realize reliable probabilistic forecasts (Nishizuka et al. 2018). We performed probabilistic forecasts for two categories: (i)  $\geq$ M-class and  $<$ M-class/non-flare events and (ii)  $\geq$ C-class and  $<$ C-class/non-flare events. We used the database of observation data taken by Geostationary Operational Environmental Satellite (GOES) and Solar Dynamic Observatory (SDO; Pesnell et al. 2012) from June 2010 to December 2015. During this period, 90% of the observed flares, such as 26 X-class, 383 M-class, and 4054 C-class flares, occurred on the solar disk. Since the number of X-class flares was too small to evaluate the prediction results, X-class flares were not predicted in this paper.

Occurrence probabilities of flares are predicted by the following steps. (i) First, we download observation data from the data archives of SDO and GOES, such as the light curves of the soft X-ray intensity, line-of-sight magnetograms, vector magnetograms, and images obtained by the 1600 Å and 131 Å filters. (ii) Second, active regions (ARs) are detected from the full-disk line-of-sight magnetograms and numbered by tracking their time evolution. (iii) For each AR, physics-based features are extracted from multiwavelength observation images, and the feature database is annotated with flare labels if an X-, M-, or C-class flare occurs within 24 h after obtaining an image. (iv) The flare occurrence probabilities in the following 24 h is predicted by supervised machine learning using a DNN for each region with a 1 h cadence. Because we investigated reliable outputs by tuning DeFN, we rename it DeFN-Reliable (DeFN-R) in this paper.

## 2.2. Observation Data and AR Features

First, we made the database from  $3 \times 10^5$  solar images of the full-disk line-of-sight magnetograms obtained by the Helioseismic and Magnetic Imager (HMI; Scherrer et al. 2012; Schou et al. 2012; Hoeksema et al. 2014) on board SDO, from which we automatically detected ARs with a reduced cadence of 1 h (see details of the detection rules described in Nishizuka et al. 2017). We neglected ARs on the limb and numbered the same ARs by tracking their time evolution. To extract various kinds of features, the frame coordinates of the detected ARs were applied to other observation images with different wavelengths, such as vector magnetograms taken by HMI/SDO and 1600 Å and 131 Å filter images by the Atmospheric Imaging Assembly (AIA; Lemen et al. 2012) on board SDO.

Next we calculated 79 features from each AR observed by multiwavelength emissions. The features are parameters based on physics that were considered to be effective for solar flare prediction in previous papers and in daily forecasting operations. The extracted features are the same as used by Nishizuka et al. (2018); for example, line-of-sight/vector magnetograms in the photosphere, brightening in the corona at 131 Å ( $T \geq 10^7$  K), and the 131 Å and X-ray emissivity 1 and 2 h before an image. The sunspot area, the magnetic flux, the number of magnetic neutral lines, and the Lorentz force were calculated from the line-of-sight/vector magnetograms. Preflare brightening in the bottom chromosphere was detected in the UV-continuum taken by the 1600 Å filter, and the coronal heating in the flaring region over  $10^7$  K was taken by the 131 Å filter, as well as the integrated X-ray emission in the range of 1-8 Å observed by GOES.

Furthermore, we standardized the feature database before the input into the DNN (e.g., Bishop 2006). The database of 2010–2015 was chronologically split into two: the dataset in 2010–2014 for training and the one in 2015 for validation and testing. These chronological datasets for training and testing are more challenging for predicting flares than the randomly shuffled and divided datasets (e.g., Bobra & Couvidat 2015; Muranushi et al. 2015; Nishizuka et al. 2017, 2018). The optimization and evaluations were repeated several times, using subsets of the training and testing datasets.

### 3. Details of DeFN-R

#### 3.1. Architecture

DeFN-R is based on algorithms of deep neural networks and composed of multilayer perceptrons. The input is the database of 79 features standardized in the preprocess, i.e., 79-dimensional vectors of features. The output is the forecast probability of each class of flares,  $p(y)$ . Here,  $y = (0, 1)$  is the class of  $\geq M$ -class flare events and  $y = (1, 0)$  is the one of  $< M$ -class or non-flare events. We calculate the two probabilities of  $\geq M$ -class flare events and  $< M$ -class or non-flare events.

The architecture of DeFN-R is fundamentally the same as that of DeFN. DeFN-R consists of several layers. At each layer of the neural networks, the input is converted to the output with a linear combination and an activation function. As the activation function, we used the rectified linear units (ReLU; Nair & Hinton 2010) for the first layer to the penultimate layer and a softmax function for the last layer,

$$\textit{Softmax}(x_i) = \frac{\exp(x_i)}{\sum_{j=1}^K \exp(x_j)}, \quad (1)$$

which gives the outputs of probabilistic forecasts. We determine the parameters in Table 1.

Figure 1(a) shows the architecture of DeFN (see Nishizuka et al. 2018, for simplified representations), while Figures 1(b) and 1(c) show the architectures of DeFN-R, which were retuned to increase BSS for  $\geq M$ -class and  $\geq C$ -class flare predictions (see Appendix A.1). DeFN-R includes simple skip connections (see also the residual network in He et al. 2015) and batch normalization represented by the notation BN (Ioffe & Szegedy 2015) to stabilize the training and improve the precision of the model. The number of nodes was investigated in the range of 79–200, and the batch size was in the range of 50–200. The architecture of DeFN-R with 5–12 layers was surveyed by attaching or detaching skip connections and dropouts. Finally, we selected the network architecture that provides representative results in the pilot experiment, as shown in Table 2.

Table 1. Symbol notations.

$x, \mathbf{x}$	Arbitrary input parameters
$y, \mathbf{y}$	Arbitrary output parameters (discrete or continuous)
$N$	Number of training samples
$K$	Number of classes/categories
$\mathbf{y}_n^* = \{ y_{nk}^*   n=1, \dots, N \}$	Correct label of $n$ th training sample
$p(\mathbf{y}_n) = \{ p(y_{nk})   n=1, \dots, N \}$	Estimated probability of $\mathbf{y}^*$

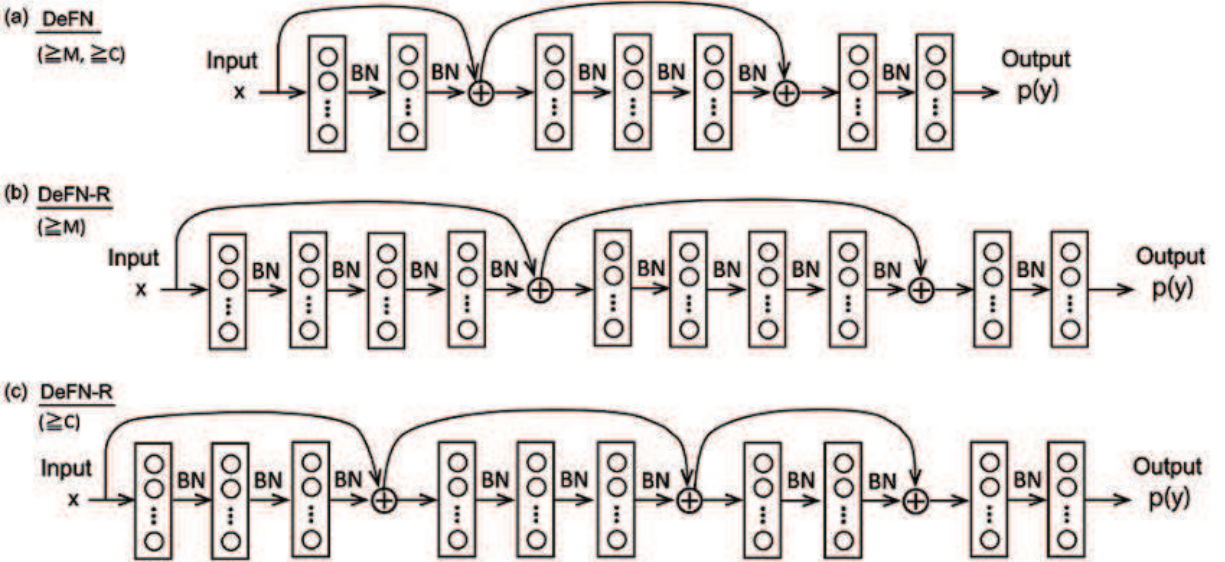


Fig. 1.— Architectures of (a) DeFN and (b), (c) DeFN-R for  $\geq M$ -class and  $\geq C$ -class flare predictions.

### 3.2. Optimization Method for DeFN-R

For classification problems, models are usually trained by optimizing parameters to minimize the cross entropy. The cross entropy between  $p(y_k^*)$  and  $p(y_k)$  is determined by the following equation:

$$J_{CE} = - \sum_{k=1}^K p(y_k^*) \log p(y_k), \quad (2)$$

where we omitted  $n$  representing the  $n$ th sample for simplicity.  $p(y_k^*)$  is the initial probability of correct labels  $y_k^*$ , i.e., 1 or 0, while  $p(y_k)$  is forecast probability. The components of  $y_k^*$  are 1 or 0, and thus,  $p(y_k^*) = y_k^*$ .

In DeFN, since the flare occurrence rate is imbalanced, the following summation of the weighted cross entropy was used as the loss function instead:

$$J_{WCE} = - \sum_{n=1}^N \sum_{k=1}^K w_k y_{nk}^* \log p(y_{nk}) \quad (3)$$

Here,  $w_k$  is the weight of each class, which was set to the inverse ratio of the class occurrence in DeFN, e.g., [1, 50] for  $\geq$ M-class flare events and [1, 12] for  $\geq$ C-class flare events. However, this results in reduced reliability. Thus, in this paper, we set the weight to be constant, i.e.,  $w_k = [1, 1]$ .

The parameters used here are summarized in Tables 1 and 2. As the method for stochastic optimization, we used adaptive moment estimation (Adam; Kingma & Jimmy 2014), which is an extension of AdaGrad, RMSprop, and AdaDelta. We used the recommended values for Adam’s hyperparameters, which are given in Table 2, because overfit hyperparameters only work with certain architectures.



Table 2. Parameter settings of DeFN-R ( $\geq$ M, C) using cross entropy as a loss function.

(a) $\geq$ M-class flares	
Loss function	Summation of cross entropy
Optimization method	Adam (learning rate = 0.001, $\beta_1 = 0.9$ , $\beta_2 = 0.999$ )
No. of nodes =	79, 150, 150, 150, 79, 150, 150, 150, 79, 150, 2
Batch size =	150
BSS =	0.298
(b) $\geq$ C-class flares	
Loss function	Summation of cross entropy
Optimization method	Adam (learning rate = 0.001, $\beta_1 = 0.9$ , $\beta_2 = 0.999$ )
No. of nodes =	79 (input), 150, 150, 79, 150, 150, 79, 150, 79, 150, 2 (output)
Batch size =	150
BSS =	0.412

## 4. Results of Probabilistic Forecasts

### 4.1. Reliability Diagram

Figures 2(a) and 3(a) respectively show reliability diagrams of probabilistic forecast results for  $\geq M$ -class flare events obtained by DeFN and DeFN-R. The blue line graph depicts the conditional expectation values of the outcome. The diagonal dotted line indicates perfect reliability, on which 95% consistency bars are attached (Brocker & Smith 2007; Jolliffe & Stephenson 2012). The 95% consistency bars show the ranges within which 95% of the conditional expectation values of the outcome given the probability would fall if it were assumed that the original data were sampled from a perfectly reliable probabilistic forecast system, namely, the null hypothesis that the probabilistic forecast is perfectly reliable is rejected with the 95% significant level if the sampled data located outside the consistency bars. The horizontal dotted line is the climatological event rate, and the line between the perfect reliability and the climatological event rate corresponds to  $BSS = 0$ . Red histograms show the number of probabilistic forecasts within bins.

Plots located above the diagonal dotted line indicate under-forecasts, while plots located below the line indicate over-forecasts. In Figure 2(a), plots are located below  $BSS=0$  line. This means that DeFN lacks reliability. On the other hand, in Figure 3(a), the reliability diagram is markedly improved, achieving  $BSS = 0.298$ . Reliability diagrams for  $\geq C$ -class flare events are shown in Figures 4(a) and 5(a), and a similar improvement is shown, although the reliability for  $\geq C$ -class flare prediction is higher ( $BSS = 0.412$ ). Larger  $BSS$  does not always correspond to a better reliability diagram. When  $BSS$  is improved, a reliability diagram sometimes gets worse. Since the number of forecasts is larger for a smaller forecast probability, it is more efficient to improve a small forecast probability; thus, the model learns to fit a lower forecast probability preferentially, and large  $BSS$  does not always coincide with a better reliability plot.

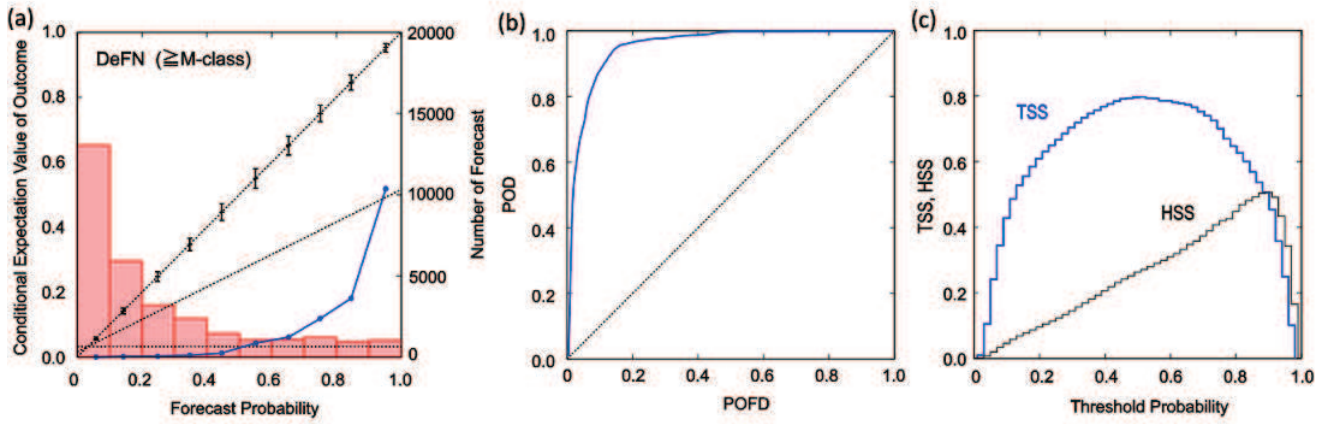


Fig. 2.— (a) Reliability diagram, (b) ROC curve, and (c) variability of TSS and HSS for probabilistic forecast of  $\geq M$ -class flares by DeFN. In panel (a), the diagonal dotted line indicates perfect reliability, on which 95% consistency bars are attached. The horizontal dotted line is the climatological event rate, and the line between the perfect reliability and the climatological event rate corresponds to BSS = 0. Red bars show the number of probabilistic forecasts within bins.

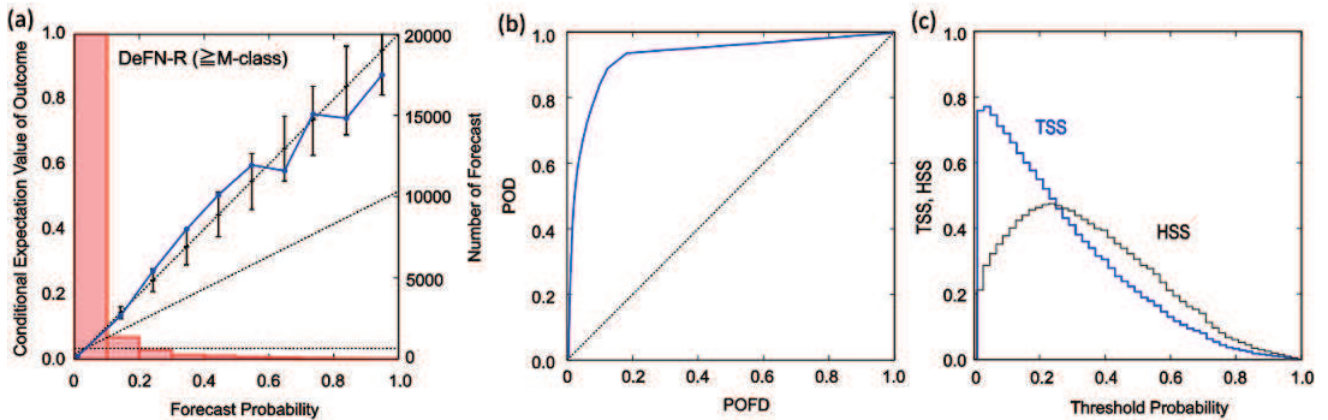


Fig. 3.— (a) Reliability diagram, (b) ROC curve, and (c) variability of TSS and HSS for probabilistic forecast of  $\geq M$ -class flares by DeFN-R.

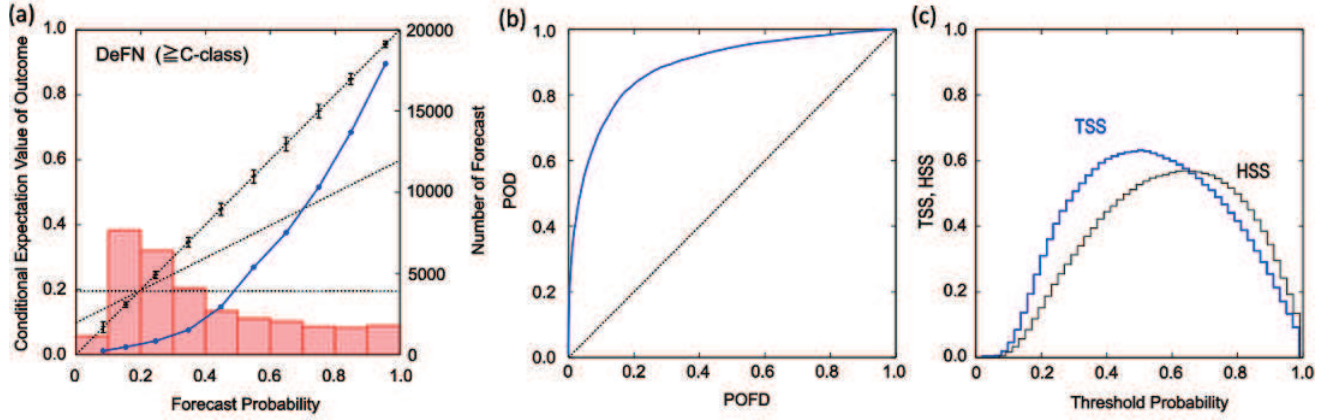


Fig. 4.— (a) Reliability diagram, (b) ROC curve, and (c) variability of TSS and HSS for probabilistic forecast of  $\geq C$ -class flares by DeFN.

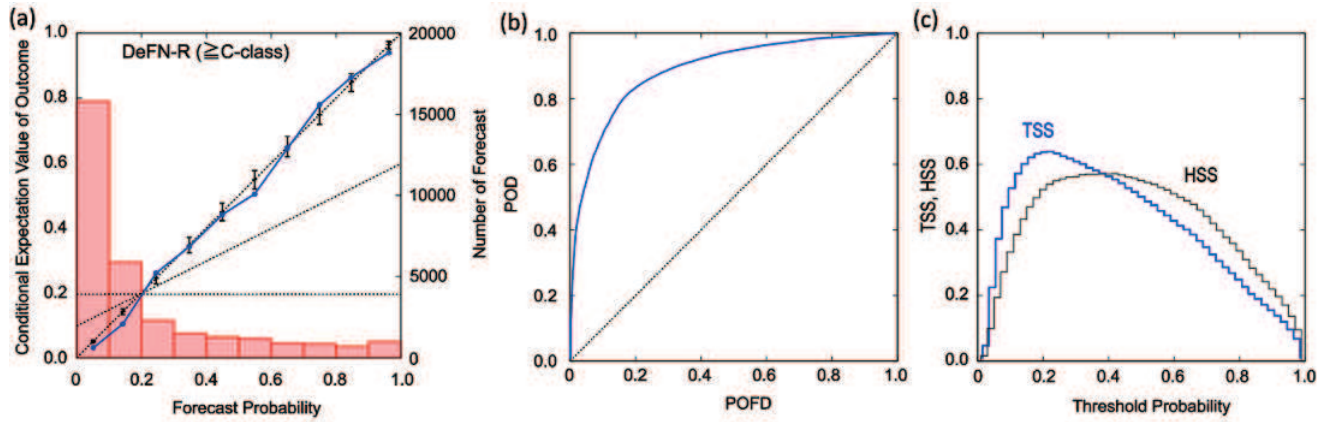


Fig. 5.— (a) Reliability diagram, (b) ROC curve, and (c) variability of TSS and HSS for probabilistic forecast of  $\geq C$ -class flares by DeFN-R.

## 4.2. Probability Threshold and ROC Curves

The output of the probabilistic forecast for a dataset is denoted as  $p(y)$ . The skill scores for deterministic forecasting require a probability threshold ( $P_{th}$ ), above which an event is predicted to occur. When we set the probability threshold, the output is determined depending on whether  $p(y)$  is greater than  $P_{th}$  or not. In DeFN or machine learning algorithms trained for deterministic forecasting, the threshold is set to 50% by default, which effectively optimizes TSS, because the errors of forecast probabilities in both categories are treated equally. In probabilistic forecast models such as DeFN-R, the threshold can be freely selected. In these models, categorical skill scores are calculated from contingency tables.

Figures 2(b) and 3(b) show the ROC curve, which tracks the performance of TSS as a function of  $P_{th}$ , because the two axes, probability of detection (POD) and probability of false detection (POFD), are the first and second terms of TSS, respectively ( $= \text{POD} - \text{POFD}$ ) (see Appendix A.2). The ROC curve shows the discrimination performance of correctly recognizing the flare occurrence. Note that the data with the maximum TSS are mostly away from the diagnostic line, but not the data closest to the point (0, 1).

Figures 2(b) and 3(b) are almost the same. For these figures, the ROC score, defined as the area under the ROC curve (AUC) (Mason & Graham 1999), is 0.96 and 0.93, and the ROC skill score (ROCSS), defined as  $\text{ROCSS} = 2\text{AUC} - 1$ , is 0.91 and 0.86, respectively. Therefore, DeFN-R improved the reliability diagram while maintaining the ROC curve. Namely, DeFN-R achieved both high discrimination performance and high reliability. Similar results are also shown in Figures 4(b) and 5(b) for  $\geq$ C-class flare probabilistic forecasts, where AUC is 0.89 and 0.89, and ROCSS is 0.77 and 0.78, respectively. In other words, the ROC curve and the variability of TSS in section 4.3 are not significantly affected by small changes of a loss function and an architecture, while a reliability diagram and BSS considerably change.

### 4.3. Variabilities of TSS and HSS

TSS is a function of threshold probability ( $P_{th}$ ), which is shown in Figures 2(c) and 3(c) for  $\geq$ M-class flare predictions. We took a threshold step of 0.02, resulting in 49 data, and a grid covering the region  $[0, 1]$  excluding the edges. In Figure 2(c), TSS continuously changes with the threshold probability and peaks at around 0.50 (50%) for DeFN. On the other hand, in Figure 3(c), TSS peaks at around 0.032 (3.2%), which is the climatological event rate of  $\geq$ M-class flare events in the datasets. In more detail, the maximum values of TSS are 0.80 and 0.77 at  $P_{th} = 0.52$  and 0.04 in Figures 2(c) and 3(c), respectively. This is confirmed by similar ROC curves of DeFN and DeFN-R. Similar findings are obtained for  $\geq$ C-class flare predictions, as shown in Figures 4(c) and 5(c). In Figure 4(c), TSS peaks at around 0.50 (50%), while it peaks near the climatological event rate of 0.196 (19.6%) in Figure 5(c). The maximum values of TSS are 0.63 and 0.64 at  $P_{th} = 0.50$  and 0.22 in Figures 4(c) and 5(c), respectively.

As a result, DeFN-R for  $\geq$ M-class and  $\geq$ C-class flare predictions shows that the maximum TSS occurs when  $P_{th}$  is approximately the climatological event rate. This is consistent with previous works by Bloomfield et al. (2012), Barnes et al. (2016), and Leka et al. (2018). It has been mathematically verified that a reliable probabilistic forecasting model has the peak of TSS at the probability threshold of the climatological event rate (Kubo 2019). In our case, DeFN-R is reliable, so the maximum TSS occurred at the climatological event rate. However, since the maximum TSS did not occur at this rate, DeFN lacks reliability. This is related to the fact that, in DeFN, the threshold is set to 50% to effectively optimize TSS and that the prior distribution is normalized by the weight of the cross entropy,  $w_k$ .

We also show the variability of the Heidke skill score (HSS) as a function of threshold probability in Figures 2(c), 3(c), 4(c), and 5(c) for comparison. The maximum values of HSS are 0.51 and 0.48 at  $P_{th} = 0.90$  and 0.24 for  $\geq$ M-class flare prediction in Figures 2(c) and 3(c), respectively. On the other hand, it is 0.57 in both Figures 4(c) and 5(c) at  $P_{th} = 0.64$  and 0.42, respectively, for  $\geq$ C-class flare prediction. The variability of HSS is also discussed in Bobra & Couvidat (2015) and Florios et al. (2018).

## 5. Summary and Discussion

We investigated the reliability performance of DeFN by changing the optimization methods of machine learning and developed a reliable probabilistic forecast model of solar flares, named DeFN-Reliable (DeFN-R). This model is trained to predict the occurrence probabilities of flares occurring within the following 24 h after observing an image in an operational setting. We compared two models with different loss functions, i.e., different weighted cross entropies with  $w_k = [1, 50]$  and  $[1, 1]$  for  $\geq$ M-class and  $<$ M-class/non-flare events and with  $w_k = [1, 12]$  and  $[1, 1]$  for  $\geq$ M-class and  $<$ M-class/non-flare events. Then, the prediction results were evaluated using reliability diagrams, ROC curves, and TSS variability as a function of threshold probability.

Comparing the two models for both  $\geq$ M-class flare events and  $\geq$ C-class flare events, we found that the reliability performance of DeFN-R varies considerably. As in DeFN, adopting weighting in the prior distribution is reasonable for a deterministic forecast, because the errors of forecast probabilities in both categories are treated equally with a threshold of 50%. On the other hand, when we compared the two models with and without weighted loss functions, the ROC curve did not change significantly, i.e., the maximum TSSs were almost the same. This indicates that, although adopting weighting on a loss function is effective for increasing TSS, the machine learning model itself is superior for prediction.

DeFN-R markedly improved reliability while keeping the ROC curve almost the same. As mathematically predicted, for reliable DeFN-R, the maximum TSS occurs at the climatological event rate. Although a DNN model using cross entropy as a loss function was considered, the reliability of the model has not been discussed. Regardless of whether or not weighting is adopted for the cross entropy, the two models are mathematically similar, although the accuracy of prediction may depend on the purpose. When we set the probability threshold at 3.6% (19.6%) for  $\geq$ M-class ( $\geq$ C-class) flare prediction, DeFN-R shows almost the same performance as DeFN. Finally, a merit of DeFN-R is that the probability threshold can be selected according to users' purposes, and DeFN-R has larger degree of freedom than deterministic forecasting models.

## A. Appendix: Evaluation Method

### A.1. Definition of Brier Skill Score for Probability Forecasting

In this paper, we used the Brier skill score (BSS) for evaluation, which is a measure of probability forecasting models. BSS is calculated from the Brier score (BS) and climatological Brier score ( $BS_c$ ) as follows:

$$BSS = \frac{BS - BS_c}{0 - BS_c}, \quad (A1)$$

$$BS = \sum_{n=1}^N (p(y_n) - y_n^*)^2, \quad (A2)$$

$$BS_c = \sum_{n=1}^N (f_i - y_n^*)^2 (i = 1, 2), \quad (A3)$$

where  $p(y_n)$  is the predicted probability and  $f_i$  is the climatological event rate. Here category  $k$  is fixed to 1, and  $y_n$  is a value for  $N$  samples. In this paper, we evaluate our model for two problems:  $\geq M$ -class and  $< M$ -class, or  $\geq C$ -class and  $< C$ -class. For  $\geq M$ -class and  $\geq C$ -class flare events,  $f_1=0.032$  and  $f_2=0.196$ , respectively. Note that probabilistic forecasting never achieves  $BS=0$ ; thus, even perfect reliability cannot achieve  $BSS=1$ .  $BSS=1$  can be achieved only by deterministic forecasts.



## A.2. Definitions of Skill Scores for Deterministic Forecasting

We used some skill scores to evaluate our deterministic forecasting of flares, by setting a probability threshold. The probability of detection (POD) or the recall, the probability of false detection (POFD), the true skill statistic (TSS), also known as the Peirce skill score or the Hanssen and Kuipers discriminant, and the Heidke skill score (HSS) were used and determined in the following way (Hanssen & Kuipers 1965; Murphy 1993; Barnes et al. 2009; Kubo et al. 2017):

$$POD = \frac{TP}{TP + FN}, \quad (\text{A4})$$

$$POFD = \frac{FP}{FP + TN}, \quad (\text{A5})$$

$$TSS = \frac{TP}{TP + FN} - \frac{FP}{FP + TN}, \quad (\text{A6})$$

$$S = \frac{a + c}{a + b + c + d}, \quad (\text{A7})$$

$$HSS = \frac{PC - PC_r}{1 - PC_r} = \frac{2S(1 - S)(POD - POFD)}{S + S(1 - 2S)POD + (1 - S)(1 - 2S)POFD}, \quad (\text{A8})$$

$$PC = \frac{a + d}{a + b + c + d} = S \cdot POD + (1 - S) \cdot POFD, \quad (\text{A9})$$

$$PC_r = \frac{(a + c)(a + b) + (b + d)(c + d)}{(a + b + c + d)^2}. \quad (\text{A10})$$

Here,  $a, b, c, d$  indicate components of a contingency table for dichotomous forecast: hits, false alarms, misses, and correct rejections, respectively.

### A.3. Robustness of DeFN-R

In this paper, we utilized a single chronological split of a database for operational evaluation, namely, datasets in 2010 - 2014 for training and those in 2015 for testing (case 0). However, it is not enough to assess the stochastic nature of DeFN-R. Although the time-series cross-validation approach can generally give optimistic assessments of a forecasting method's performance, it allows multiple runs to be made, so we computed standard deviations of all the skill scores as a function of the probability threshold.

Here, we considered a few more splits, in the chosen operational settings approach. We considered the following cases: (1) 2010 - 2013 for training and 2014 - 2015 for testing, (2) Jun 2010 - Mar 2014 for training and Apr 2014 - Dec 2015 for testing, (3) Jun 2010 - Jun 2014 for training and Jul 2014 - Dec 2015 for testing, (4) Jun 2010 - Sep 2014 for training and Oct 2014 - Dec 2015 for testing, (5) Jun 2010 - Mar 2015 for training and Apr 2015 - Dec 2015 for testing, and (6) Jun 2010 - Jun 2015 for training and Jul 2015 - Dec 2015 for testing. Although the time-series cross-validation is more reasonable for model selection, this is out of scope.

The prediction results are shown in Table 3 and Figures 6 and 7. When the size of the training dataset was reduced in cases 1 - 3, BSS decreased as shown in Table 3. This is probably because the solar maximum occurred in 2014, and it appears that we had insufficient training samples when we reduced the number of samples from the datasets in 2014. In cases 4 and 5, BSS was almost the same as that of case 0 except for case 5 for  $\geq M$ -class events. In case 6, BSS increased.

Figures 6 and 7 show the results for cases 0 - 6 described above in the form of reliability diagrams, ROC curves, and TSS vs probability threshold curves and for  $\geq M$  or  $< M$ -class and  $\geq C$  or  $< C$ -class flare predictions of DeFN-R. Cases 1, 2, and 5 for  $\geq M$ -class flare prediction show a lower reliability than the other cases, as can be seen in Figure 6(a). The reliability diagrams in Figures 6(a) and 7(a) vary with the case, mainly in the range of 0.4 - 1.0, but the variation is almost within the 95% consistency bars in Figures 3(a) and 5(a). Therefore, our prediction results in case 0 obtained using our database are reasonably robust.

Table 3. BSS in cases 0 - 6 for  $\geq$ M-class and  $\geq$ C-class flare predictions by DeFN-R.

	$\geq$ M-class flares		$\geq$ C-class flares	
	BSS	climatology	BSS	climatology
Case1 (test: 2014 Jan -)	0.2574	0.0353	0.3530	0.2161
Case2 (test: 2014 Apr -)	0.2337	0.0318	0.3609	0.2124
Case3 (test: 2014 Jul -)	0.2529	0.0327	0.3738	0.2038
Case4 (test: 2014 Oct -)	0.2849	0.0350	0.4110	0.1982
Case0 (test: 2015 Jan -)	0.2977	0.0324	0.4107	0.1958
Case5 (test: 2015 Apr -)	0.2559	0.0309	0.4268	0.1954
Case6 (test: 2015 Jul -)	0.3017	0.0350	0.4558	0.1804

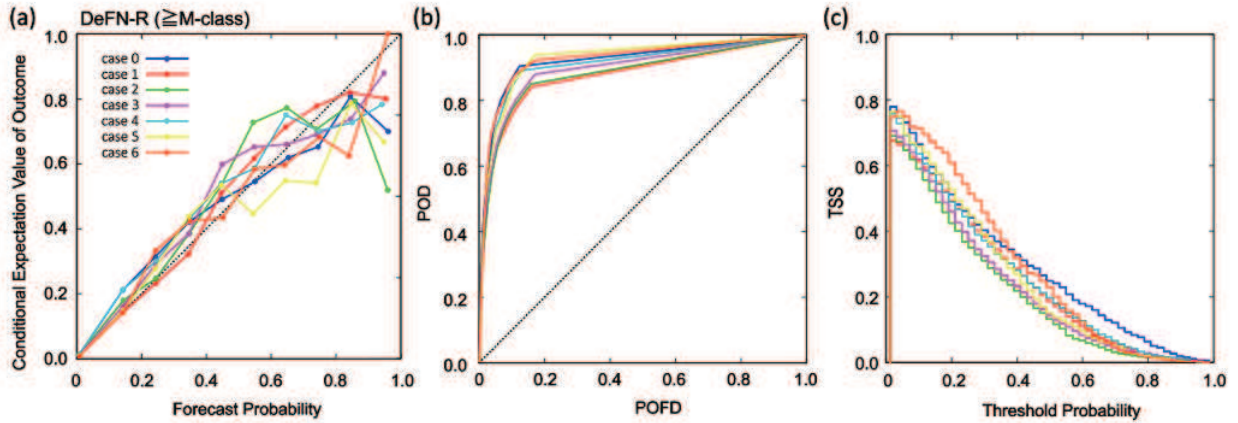


Fig. 6.— (a) Reliability diagrams, (b) ROC curves, and (c) variability of TSS for probabilistic forecast of  $\geq$ M-class flares by DeFN-R in cases 0 - 6.

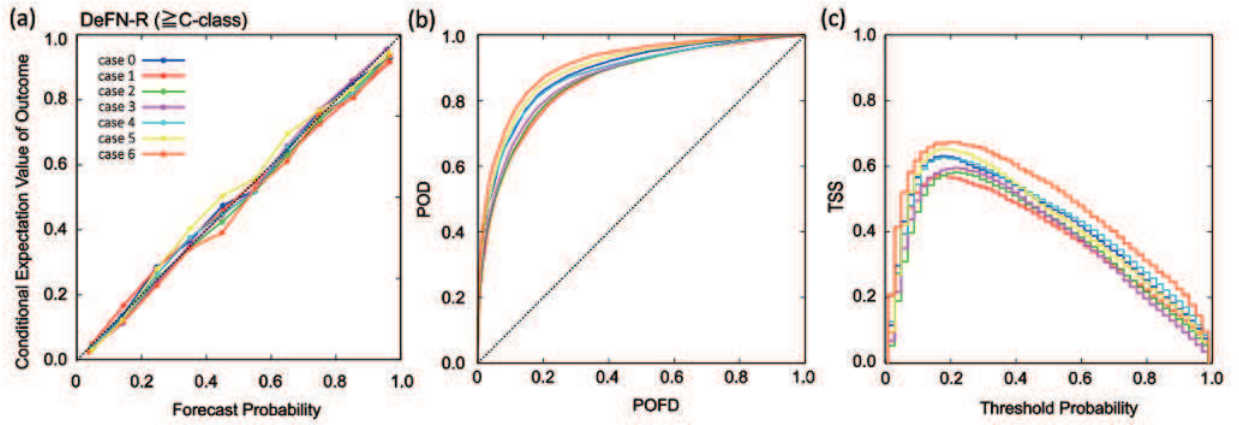


Fig. 7.— (a) Reliability diagrams, (b) ROC curves, and (c) variability of TSS for probabilistic forecast of  $\geq C$ -class flares by DeFN-R in cases 0 - 6.

The data used here are courtesy of NASA/SDO, the HMI & AIA science teams, Joint Science Operations Center (JSOC), as well as GOES team. This work was supported by KAKENHI grant Number JP18H04451.

## REFERENCES

- Ahmed, O. W., Qahwaji, R., Colak, T., Higgins, P. A., Gallagher P. T., & Bloomfield D. S., 2013, *Sol. Phys.*, 283, 157
- Al-Ghraibah, A., Boucheron, L. E., & McAteer, R. T. J. 2015, *A&A*, 579, A64
- Alipour, N., Mohammadi, F., & Safari, H., 2019, *ApJS*, 243, 20
- Barnes, L. R., Schults, D. M., Gruntfest, E. C., Hayden, M. H., & Benight, C. C., 2009, *Weather and Forecasting*, 24, 1452
- Barnes, G., et al., 2016, *ApJ*, 829, 89
- Benvenuto, F., Piana, M., Campi, C., & Massone, A. M., 2018, *ApJ*, 853, 90
- Bishop, C. M., 2006, *Pattern Recognition and Machine Learning (Information Science and Statistics)*, Springer Science+Business Media, LLC
- Bloomfield, D. S., Higgins, P. A., McAteer, R. T. J., & Gallagher, P. T., 2012, *ApJ*, 747, L41
- Bloomfield, D. S., Gallagher, P. T., Marquette, W. H., Milligan, R. O., & Canfield, R. C., 2016, *Sol. Phys.*, 291, 411
- Bobra, M. G., & Couvidat, S., 2015, *ApJ*, 798, 135
- Boucheron, L. E., Al-Ghraibah, A., & McAteer, R. T. J., 2015, *ApJ*, 812, 51
- Brocker, J. & Smith, L. A., 2007, *Wea. Forecasting*, 22, 651
- Campi, C., Benvenuto, F., Massone, A. M., Bloomfield, D. S., Georgoulis, M. K., & Piana, M., *ApJ*, 883, 150
- Chen, Y., et al., 2019, *Space Weather*, 17, 1404
- Colak, T., & Qahwaji, R., 2009, *Space Weather*, 7, S06001

- Crown, M. D., 2012, *Space Weather*, 10, S06006
- Devos, A., Verbeeck, C., & Robbrecht, E., 2014, *J. Space Weather Space Clim.*, 4, A29
- Domijan, K., Bloomfield, D. S., & Pitié, F., 2019, *Sol. Phys.*, 294, 6
- Florios, K., Kontogiannis, I., Park, S.-H., Guerra, J. A., Benvenuto, F., Bloomfield, D. S., & Georgoulis, M. K., *Sol. Phys.*, 2018, 293 (2), 28
- Gallagher, P. T., Moon, Y.-J., & Wang, H., 2002, *Sol. Phys.*, 209, 171
- Gneiting, T., Balabdaoui, F., & Raftery, A. E., 2007, *J. R. Statist. Soc. B*, 69, 243
- Hanssen, A. W., & Kuipers, W. J. A., 1965, *Mededelingen en verhandelingen*, 81, Royal Netherlands Meteorological Institute
- Harvey, L. O., Hammond, K. R., Lusk, C. M., & Mross, E. F., 1992, *Mon. Wea. Rev.*, 120, 863
- He, K., Zhang, X., Ren, S., & Sun, J., 2015, Deep Residual Learning for Image Recognition, in arXiv: 1512.03385, 2015. <http://arxiv.org/abs/1512.03385>
- Higgins, P. A., Gallagher, P. T., McAteer, R. T. J., & Bloomfield, D. S., 2011, *Advances in Space Research*, 47, 2105
- Hoeksema, J. T., et al., 2014, *Sol. Phys.*, 289, 3483
- Huang, X., Wang, H., Xu, L., Liu, J., Li, R., & Dai, X., 2018, *ApJ*, 856, 7
- Ioffe, S. & Szegedy, C., 2015, in Proc. 32nd International Conf. on Machine Learning, held in Lille, France in July 2015, 37, 448
- Jolliffe, I. T. & Stephenson, D. B., 2012, *Forecast Verification: A Practitioner's Guide in Atmospheric Science*, Second edition, John Wiley and Sons Ltd.
- Jonas, E., Bobra, M., Shankar, V., Hoeksema, J. T., & Recht, B., 2018, *Sol. Phys.*, 293, 48
- Kingma, D., & Jimmy, B., 2014, arXiv preprint arXiv:1412.6980.
- Kubo, Y., Den, M., & Ishii, M., 2017, *J. Space Weather Space Clim.*, 7, A20
- Kubo, Y., 2019, *J. Space Weather Space Clim.*, 9, A17
- Lee, K., Moon, Y.-J., Lee, J.-Y., et al., 2012, *Sol. Phys.*, 281, 639

- Lee, K., Moon, Y.-J., & Nakariakov, V. M., 2016, *ApJ*, 831, 131
- Leka, K.D., Barnes, G., & Wagner, E., 2018, *Space Weather Space Clim.*, 8, A25
- Leka, K. D., et al. 2019, *ApJS*, 243, 36
- Lemen, J. et al. 2012, *Sol. Phys.*, 275, 17
- Li, X., Zheng, Y., Wang, X., & Wang, L., 2020, *ApJ*, 891, 10
- Lim, D. et al., 2019, *ApJ*, 885, 35
- Lim, D., et al., 2019, *JKAS*, 52, 133
- Liu, C., Deng, N., Wang, J.T.L., & Wang, H. 2017, *ApJ*, 843, 104
- Liu, H., Liu, C., Wang, J. T. L., & Wang, H., 2019, *ApJ*, 877, 121
- Mason, I., 1982, *Aust. Meteor. Mag.*, 30, 291
- Mason, S. J., & Graham, N. E., 1999, *Wea. Forecasting*, 14, 713
- McCloskey, A. E., Gallagher, P. T., & Bloomfield, D. S., 2016, *Sol. Phys.*, 291, 1711
- McCloskey, A. E., Gallagher, P. T., & Bloomfield, D. S., 2018, *Space Weather Space Clim.*, 8, A34
- Moon, Y.-J., Choe, G. S., Yun, H. S., & Park, Y. D., 2001, *JGR*, 106, 29951
- Moon, Y. -J., Chae, J., Choe, G. S., Wang, H., Park, Y. D. & Cheng, C. Z., 2004, *J. Korean Astron. Soc.*, 37, 41
- Muranushi, T., Shibayama, T., Muranushi, Y. H., Isobe, H., Nemoto, S., Komazaki, K. & Shibata, K., 2015, *Space Weather*, 13
- Murphy, A. H., 1993, *Weather and Forecasting*, 8, 282
- Murray, S. A., Bingham, S., Sharpe, M., & Jackson, D. R., 2017, *Space Weather*, 17, 577
- Nair, V. & Hinton, G. E., 2010, in *Proc. of the 27 th International Conference on Machine Learning*, Haifa, Israel, 2010.
- Nishizuka, N., Sugiura, K., Kubo, Y., Den, M., Watari, S., & Ishii, M., 2017, *ApJ*, 835, 156
- Nishizuka, N., Sugiura, K., Kubo, Y., Den, M., & Ishii, M., 2018, *ApJ*, 858, 113

- Panos, B., & Kleint, L., 2020, ApJ, 891, 17
- Park, E., Moon, Y.-J., Shin, S., Yi, K., Lim, D., Lee, H., & Shin, G., 2018, ApJ, 869, 91
- Park, S. -H., et al., 2020, ApJ, 890, 124
- Pesnell, W., et al. 2012, Sol. Phys., 275, 229
- Primo, C., Ferro, C. A. T., Jolliffe, I. T., & Stephenson, D. B., 2009, Mon. Wea. Rev., 137, 1142
- Qahwaji, R. & Colak, T., 2007, Sol. Phys., 241, 195
- Raboonik, A., Safari, H., Alipour, N., & Wheatland, M. S., 2017, ApJ, 834, 11
- Sadykov, V. M., & Kosovichev, A. G., 2017, ApJ, 849, 148
- Scherrer, P. H., et al., 2012, Sol. Phys., 275, 207
- Schou, J., et al., 2012, Sol. Phys., 275, 229
- Stanski, H. R., Wilson, L. J., & Burrows, W. R., 1989, WWW Tech. Rep. 8, WMO/TD 358, 114 pp.
- Swets, J. A., 1973, Science, 182, 990
- Wang, J., Liu, S., Ao, X., Zhang, Y., Wang, T., & Liu, Y., 2019, ApJ, 884, 175
- Wheatland, M. S., 2000, ApJ, 536, L109
- Wheatland, M. S., 2005, Space Weather, 3, S07003
- Yi, K., Moon, Y.-J., Shin, G., & Lim, D., 2020, ApJ, 890, L5
- Yuan, Y., Shih, F. Y., Jing, J., & Wang, H.-M., 2010, RAA, 10, 785
- Zheng, Y., Li, X., & Wang, X., 2019, ApJ, 885, 73